INTERNATIONAL ATOMIC ENERGY AGENCY
UNITED NATIONS EDUCATIONAL, SCIENTIFIC AND CULTURAL ORGANIZATION
INTERNATIONAL CENTRE FOR THEORETICAL PHYSICS
I.C.T.P., P.O. BOX 586, 34100 TRIESTE, ITALY. CABLE CENTRATOM TRIESTE

H4.SMR/645-11

**SCHOOL ON PHYSICAL METHODS FOR THE STUDY OF THE UPPER AND LOWER ATMOSPHERE SYSTEM**

**26 October - 6 November 1992**
**Miramare - Trieste, Italy**

***Atmospheric Coupling Mechanisms***

**Marvin A. Geller**
**State University of New York**
**Stony Brook, NY**
**USA**



# Atmospheric Coupling Mechanisms

Marvin A. Geller
Institute for Terrestrial and Planetary Atmospheres
State University of New York at Stony Brook
Stony Brook, New York 11777
USA

## 1. Introduction

This lecture will first show some observations of the lower and middle atmosphere and compare these with calculations in which atmospheric wave dynamics is not present. Some of the ways in which the momentum deposition by atmospheric wave motions that have their source in the troposphere improve the agreement between modeled atmospheric structure and observations are as follows:

(1) the winter and summer jets become closed;

(2) the winter stratosphere is made warmer;

(3) the meridional temperature gradient is such that the winter mesopause temperatures are warmer than those in the summer; and

(4) a meridional and vertical circulation is induced that is consistent with observed constituent distributions.

## 2. Gravity Waves

The first wave type to be discussed are internal gravity waves. these are atmospheric waves with frequencies that lie above that of buoyancy oscillations and less than $2\pi$ divided by the Coriolis parameter. They can be ducted by temperature variations. Also, vertical variations of the horizontal wind affect their vertical propagation. For instance, they are absorbed at critical levels where heir Doppler-shifted frequency becomes zero. This is thought to iffect the distribution of turbulence in the middle atmosphere as well as constituent distributions. Gravity waves are forced by a number of mechanisms including orographic forcing, convective activity, shear instability, and geostrophic adjustment.

3. Tides

Atmospheric tides are global scale waves that are forced either thermally or gravitationally with an astronomically determined period. The principal tidal components are the solar diurnal and semidiurnal tides as well as the lunar semidiurnal tide. The amplitude of the tides grow with altitude roughly exponentially up through the mesosphere. They can be a source of turbulence for the upper atmosphere. Their momentum deposition at high altitudes may also become important. They provide the dynamic forcing for dynamo currents in the E region.

4. Extratropical Planetary Waves

Surface continent-ocean distributions give rise to thermal and orographic forcing of planetary waves. These planetary waves are important in the troposphere but become dominant in the middle atmosphere. Stratospheric wind systems affect the vertical propagation of planetary waves such that stationary planetary waves cannot propagate vertically through the summer easterlies. Their vertical propagation is also inhibited by very strong westerly winds. These properties help to explain seasonal and interhemispheric variations in planetary wave structure. Planetary waves interact with the mean zonal flow. The weaker forcing of planetary waves in the Southern Hemisphere helps to explain the different nature of the annual cycle in the dynamics of the Northern and Southern Hemispheres. Planetary wave interactions with the mean zonal flow produce stratospheric warmings. Traveling planetary waves with two day, five day, sixteen day, and other periods are also observed.

5. Equatorial Waves

Close to the Equator, the Coriolis parameter ( $f = 2\Omega\sin\phi$ ), goes to zero. This condition permits the existence of special equatorially trapped waves. It is thought that these waves are being constantly excited by tropical convection. These waves, along with gravity waves, are thought to provide eastward and westward momentum fluxes into the stratosphere, thus driving the quasi-biennial oscillation (QBO) in the lower stratosphere and the semiannual oscillation in the upper stratosphere. The QBO is an excellent example of an atmospheric oscillation that is unrelated to a forcing with a similar period. The period of the QBO is variable, and little is known about what is responsible for these variations. There is a suggestion, however, that these variations may be due to variations in tropical sea surface temperatures (SST's). Ozone variations are seen that are related to the QBO. An SST response is also seen in the ozone field.

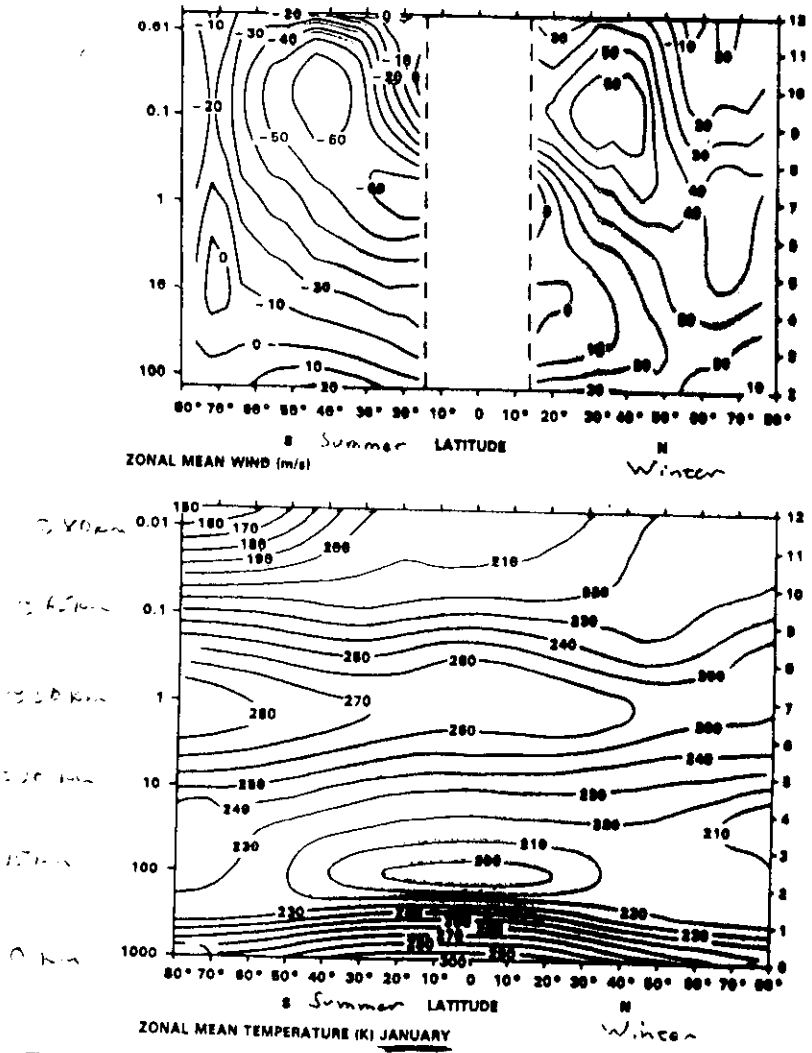


**Figure 6-1.** Cross sections (pressure (mbar)-latitude) of zonal mean geostrophic wind ($ms^{-1}$) and zonal mean temperature (K) for the average over 5 years of the monthly means for January. The data are from the combined SCR/PMR retrieval made at the University of Oxford for the period January 1973 to December 1974 and July 1975 to June 1978. (Supplied by J.J. Barnett and M. Corney).

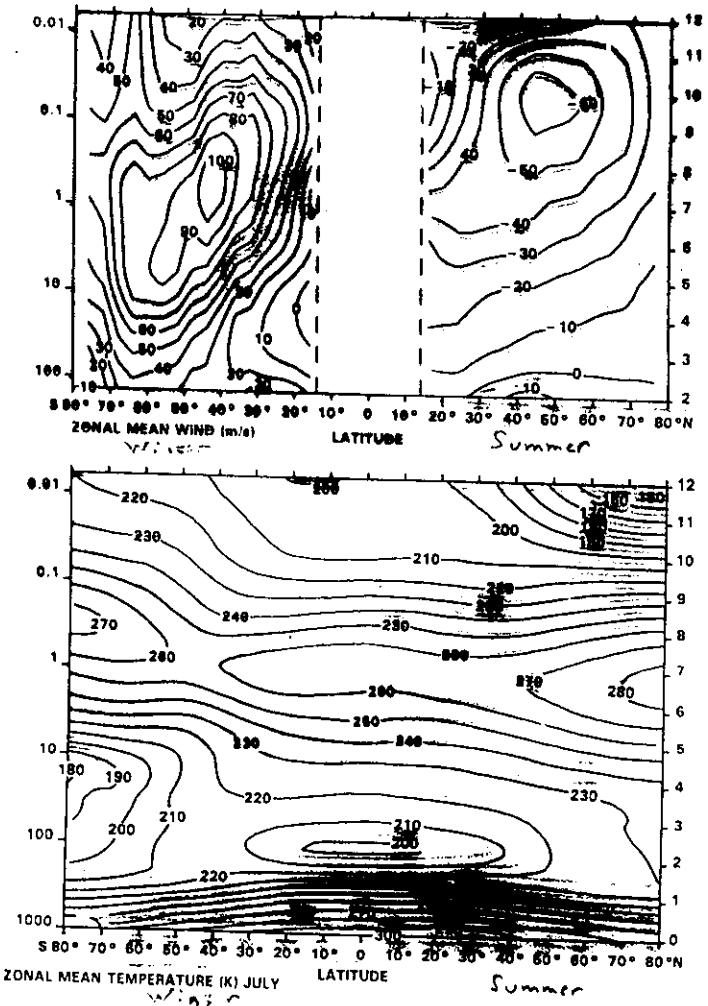


Figure 6-2. As Figure 6-1 but for July.

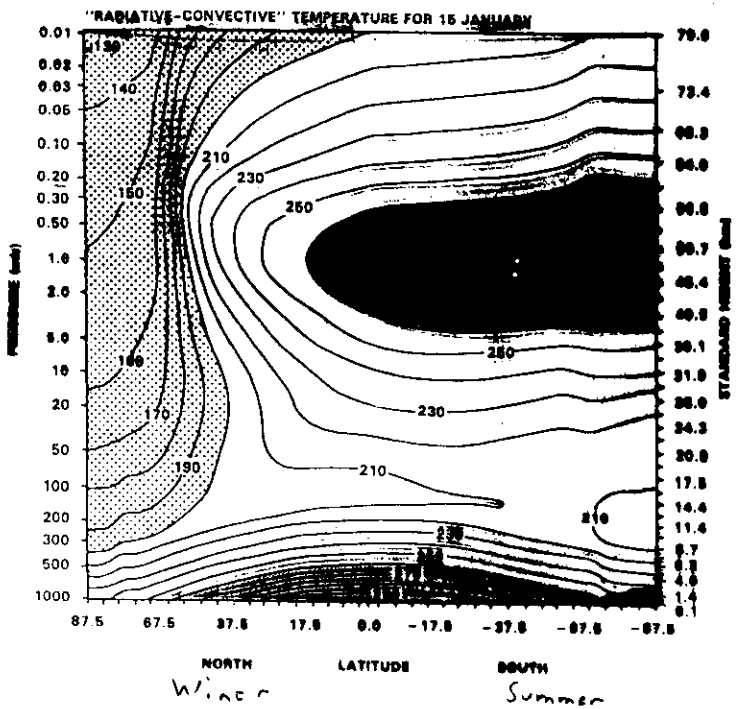


**Figure 6-30.** Time-dependent "radiatively-determined" temperature T, for 15 January 1968 from the calculation of Fels and Schwarzkopf (1985). The surface temperatures are prescribed at their seasonally-varying observed values. Cloudiness, and ozone below 35 km, are prescribed at annual-mean values, as in Fels *et al.* (1980); ozone above 35 km is allowed to "float", in response to temperature variations, towards a crude photochemical equilibrium. Details of the water vapor prescription are relatively standard and are described in Fels and Schwarzkopf (1985). (From Manabe and Hunt, 1984).

Radiative Equilibrium ⇒

Radiative Heating = Radiative Cooling

January

WARM

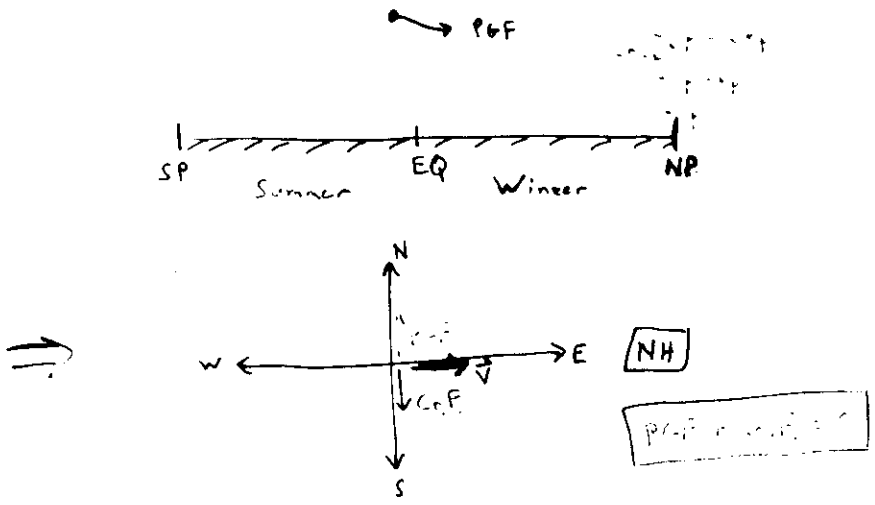


## Geostrophic Wind Relations

$$u = -\frac{g}{f}\left(\frac{\partial Z}{\partial y}\right)_p \quad \text{and} \quad v = \frac{g}{f}\left(\frac{\partial Z}{\partial x}\right)_p$$

## Thermal Wind Relations

$$\frac{\partial u}{\partial \ln p} = \frac{R}{f}\left(\frac{\partial T}{\partial y}\right)_p \quad \text{and} \quad \frac{\partial v}{\partial \ln p} = -\frac{R}{f}\left(\frac{\partial T}{\partial x}\right)_p$$

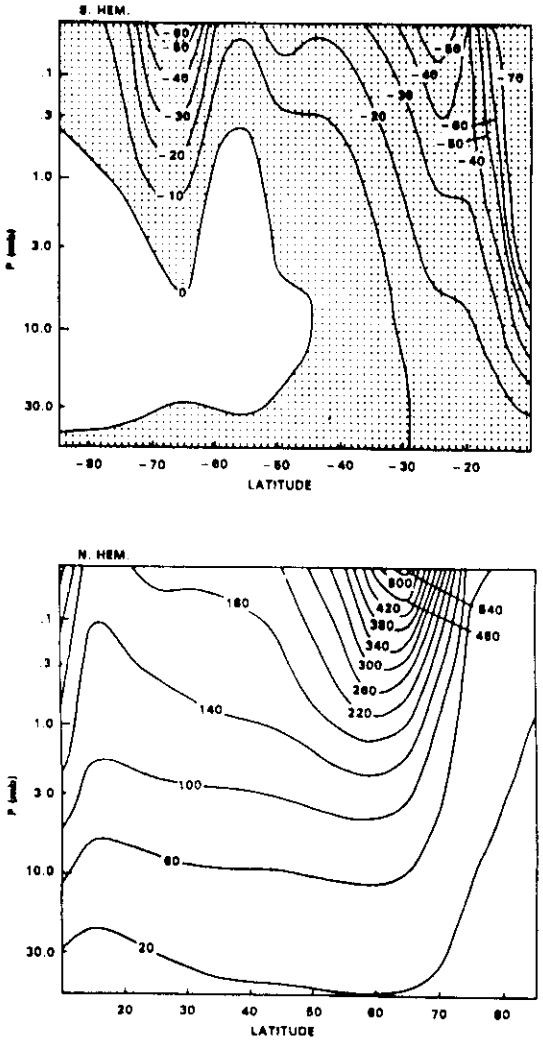


**Figure 6-31.** Geostrophic winds U (θ,P) calculated from the January 15 temperatures of Figure 6-30. The value of U (θ, 50 mb) is taken from Oort and Rasmussen, and the thermal wind equation integrated upward from 50 mb. The contours have been modestly handsmoothed. [After Fels and Schwarzkopf, 1986].

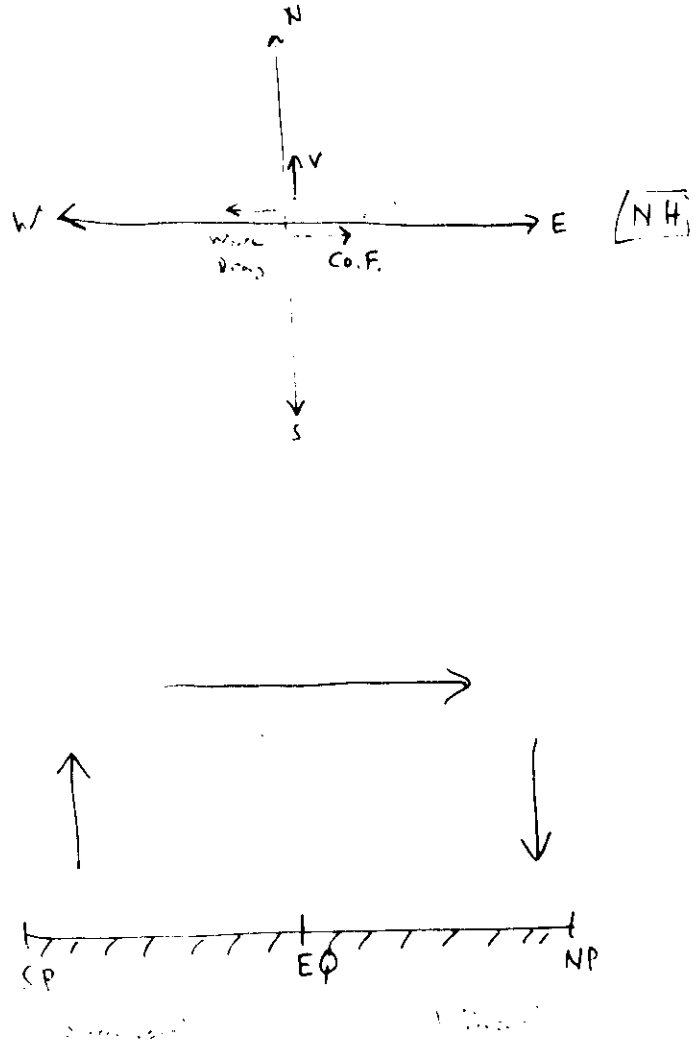

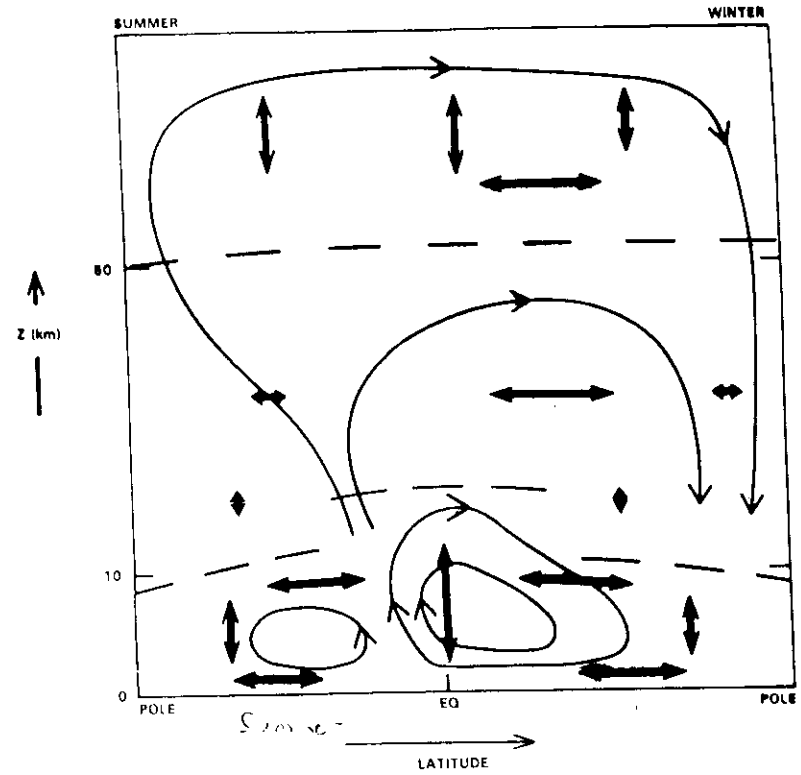


**Figure 6-55.** Schematic illustration of zonally-averaged transport processes up to the mesopause. Single arrows: mean circulation; double arrows: quasi-horizontal and vertical diffusion. See text for discussion.

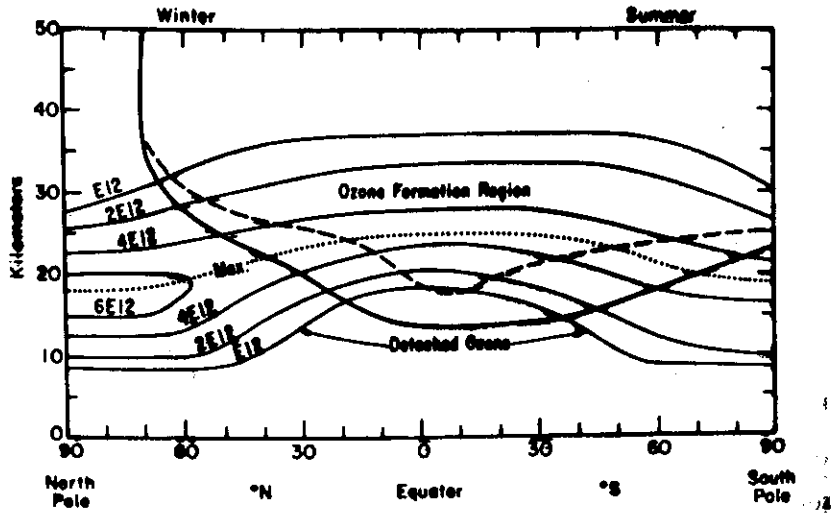


**Fig. 11.11** Longitudinal mean ozone concentration in units of molecules $cm^{-3}$ (4E12 means $4 \times 10^{12}$) for mid-January. See text for further explanation. (After Climatic Impact Committee, 1975.)

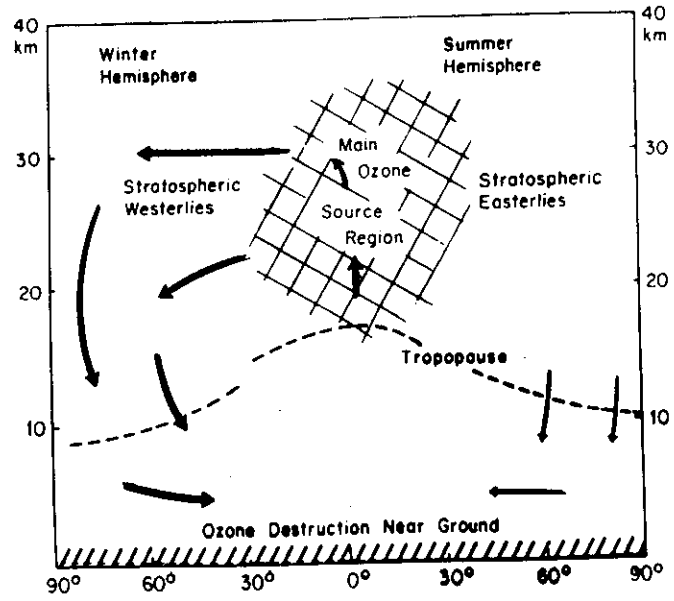


Fig. 11.12 Schematic illustration showing sources, sinks, and mass transport of ozone. (After

## Buoyancy Oscillations

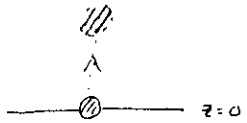


Consider an air parcel displaced vertically from its equilibrium position.

n. of Motion

$$\frac{d^2z}{dt^2} = -\frac{1}{\rho}\frac{\partial p'}{\partial z} - g \qquad (-gp')$$

( ) — parcel
( )′ — environment

$$\frac{d^2z}{dt^2} = g\left(\frac{\rho' - \rho}{\rho}\right) = g\left(\frac{T - T'}{T'}\right)$$

(assuming $p = p'$ and $p = \rho RT$)

$$\approx g\left(\frac{\left(T_0 - \frac{g}{c_p}z\right) - \left(T_0 + \frac{\partial T}{\partial z}\Big|_0 z\right)}{T_0}\right)$$

$$= -\frac{g}{T_0}\left[\frac{g}{c_p} + \frac{\partial T_0}{\partial z}\right]z$$

$$\therefore \quad \frac{d^2z}{dt^2} + N^2 z = 0$$

Harmonic oscillations with period $\frac{2\pi}{N}$

N is the Brunt-Vaisala frequency

## Geometric Derivation of Internal Gravity Waves

Consider a corrugated sheet being pulled horizontally at a speed c through a stratified fluid.

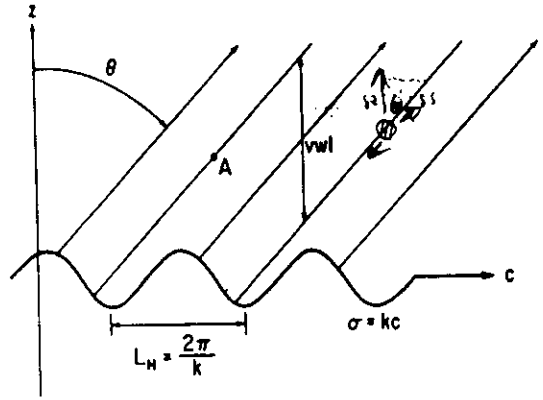


Corrugated lower surface moving through a fluid.

Wave motions are excited in the fluid above the plate.

$$F = -N^2 \delta z \cos\theta$$

Also, $\delta z = \delta s \cos\theta$, so

$$F = -N^2 \cos^2\theta \, \delta s$$

$$\therefore \quad \frac{d^2\delta s}{dt^2} = -N^2 \cos^2\theta \, \delta s$$

Assume $\delta s \propto e^{i\sigma t}$ $\quad \delta s \propto e^{i\sigma t}$

$\Rightarrow \quad \sigma^2 = N^2\cos^2\theta = K^2c^2$

$\therefore$ $Kc$ determines the angle $\theta$.

But, $\tan\theta = L_H/L_v = \ell/K \qquad \left(\ell = \frac{2\pi}{L_v},\ K = \frac{2\pi}{L_H}\right)$

$$\therefore \quad \tan^2\theta = \frac{\ell^2}{K^2} = \frac{1-\cos^2\theta}{\cos^2\theta} = \frac{1-\frac{K^2c^2}{N^2}}{\frac{K^2c^2}{N^2}}$$

$\Rightarrow$ Dispersion Relation $\quad \ell^2 = \left(\frac{N^2}{K^2c^2} - 1\right)K^2$

$$= \left(\frac{N^2}{\sigma^2} - 1\right)K^2$$

Therefore, vertical propagation requires $\sigma^2 < N^2$

Also, $\quad \sigma = \pm \dfrac{NK}{(K^2+\ell^2)^{1/2}}$

$$\left.\begin{aligned} c_{px} &= \frac{\sigma}{K} = \pm \frac{N}{(K^2+\ell^2)^{1/2}} \\ c_{pz} &= \frac{\sigma}{\ell} = \pm \frac{NK/\ell}{(K^2+\ell^2)^{1/2}} \end{aligned}\right\} \text{phase velocity}$$

$$\left.\begin{aligned} c_{gx} &= \frac{\partial\sigma}{\partial K} = \pm \frac{N\ell^2}{(K^2+\ell^2)^{3/2}} \\ c_{gz} &= \frac{\partial\sigma}{\partial\ell} = \pm \frac{-NK\ell}{(K^2+\ell^2)^{3/2}} \end{aligned}\right\} \text{group velocity}$$

Note that as $\sigma \to 0$, $\ell \to \infty$, or $L_v \to 0$. This will act to prevent vertical propagation.

Note the following:

(1) For nondissipative plane waves,

$\rho |\vec{v}|^2 =$ constant, but $\rho \sim e^{-z/H}$

$\Rightarrow |\vec{v}| \sim e^{+z/2H}$. Also $|T| \sim e^{+z/2H}$.

$\Rightarrow$ Wave Breaking

(2) If there is a mean flow in the x-direction,

$\sigma \rightarrow \sigma - k \cdot U$

$\Rightarrow \ell^2 = \left( \frac{N^2}{(\sigma - kU)^2} - 1 \right) K^2$

So, $\theta = \tan^{-1}(\ell/K) \Rightarrow$ ducting will tend to occur when $N^2 \rightarrow \infty$ or when $U \rightarrow \sigma/K (= c_{px})$ ≤ critical levels

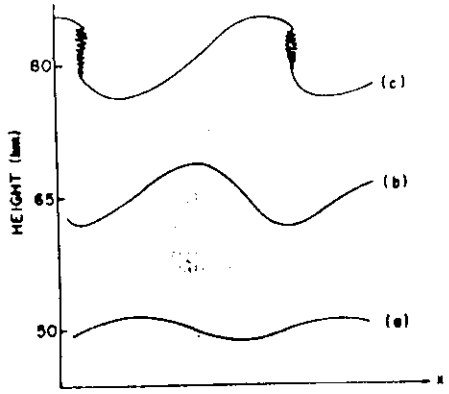


**Fig. 4.17.** Schematic diagram illustrating the breaking of vertically propagating internal gravity waves in the mesosphere. The curves labeled (a), (b), and (c) denote material surfaces. At the level of (a) and (b) the linear nondissipative theory of Section 4.6.1 is approximately valid. At the level of (c) nonlinear effects are important, with irreversible deformation of previously wavy material surfaces, and turbulence near the wave crests, presumably followed by small-scale mixing and dissipation.

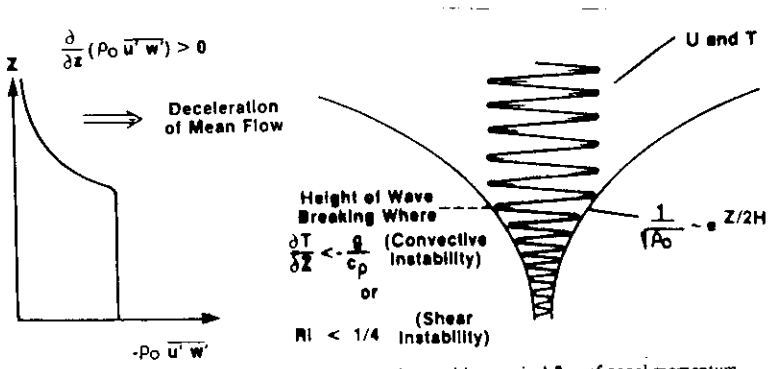


Fig. 12. Schematic of gravity wave breaking and the resulting vertical flux of zonal momentum.

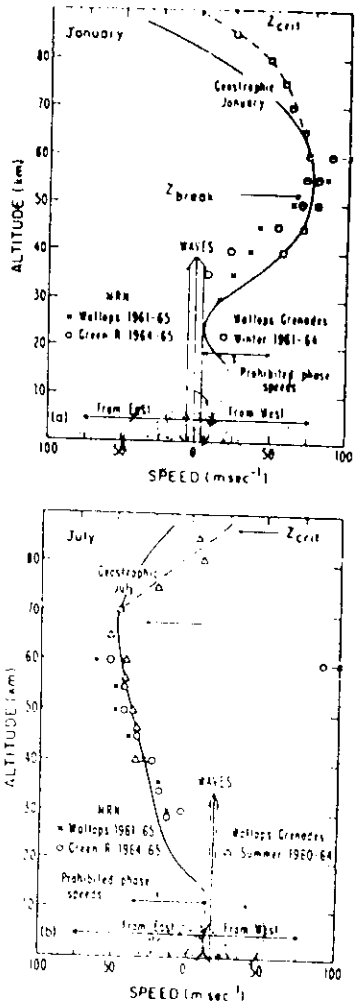


Fig. 10. Schematic illustrating the allowed and prohibited phase speeds for gravity waves at Wallops Island for winter and summer [*Lindzen*, 1981]. Note that the summer wind profile prevents stationary waves from entering the middle atmosphere.

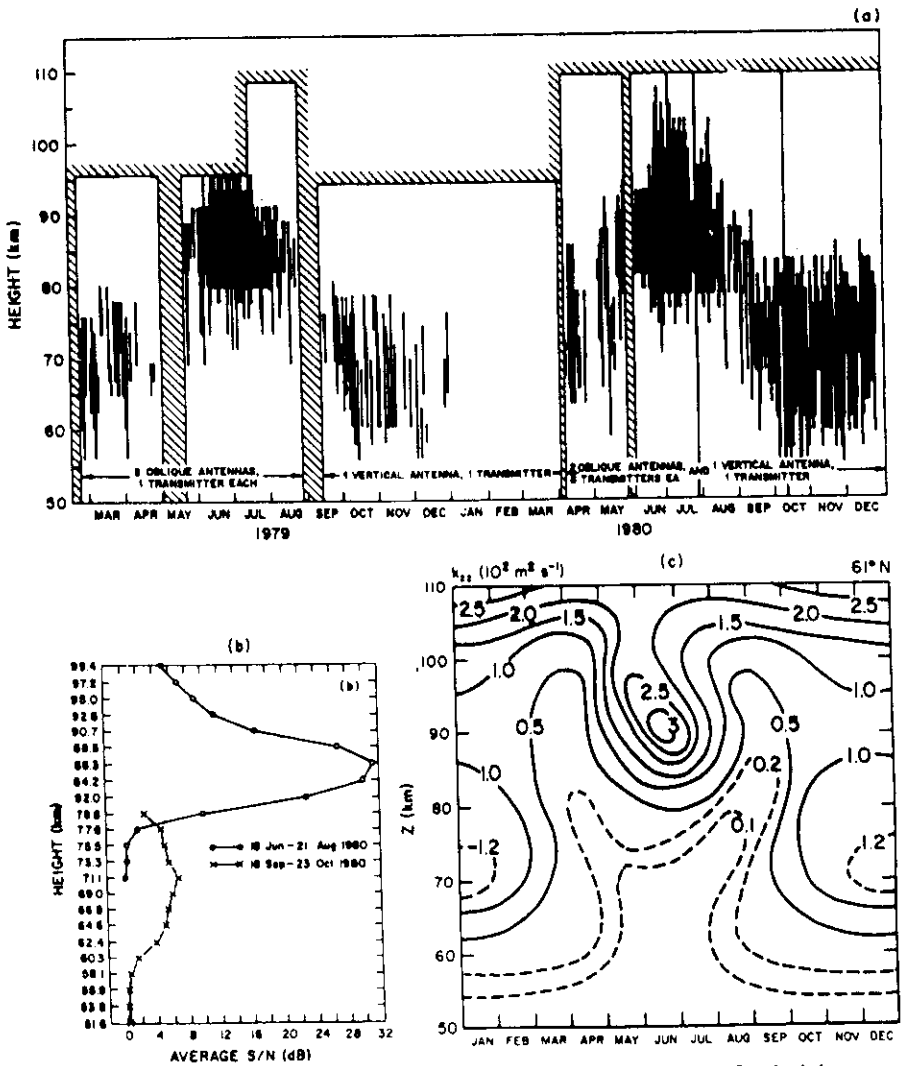


Fig. 10. (a) Height distribution of MST radar echoes at Poker Flat (65°N) as a function of season. Cross-hatched areas denote periods and altitudes for which no data are available [from *Balsley et al.*, 1983]. (b) Vertical profiles of radar echo signal to noise ratio for summer (July 18 to August 21, 1980, average) and fall (September 16 to October 23, 1980) [*Balsley et al.*, 1983]. (c) Computed vertical profile of eddy diffusion coefficient as a function of season for 61°N.

## Gravitational Tides

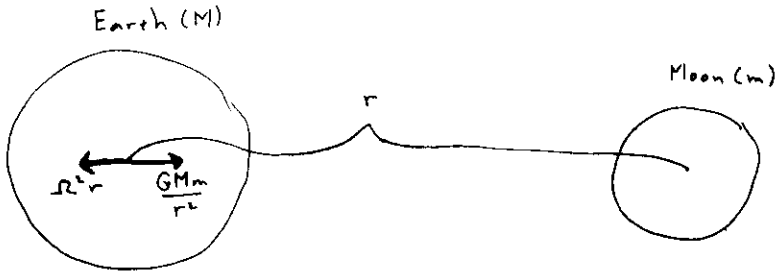


Gravity Force = Centrifugal Force

at the center of the Earth

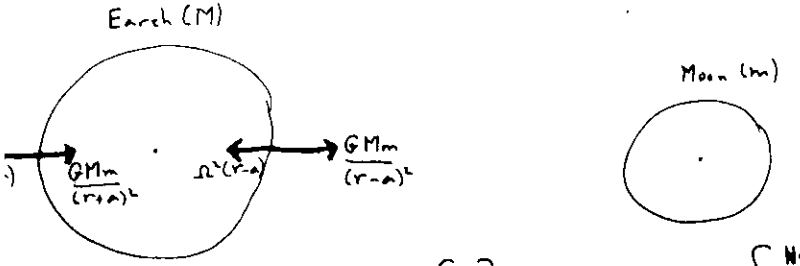


Gravity Force $\left\{ > \atop < \right\}$ Centrifugal Force $\left\{ \begin{array}{l} \text{Near the Moon} \\ \text{Far from the Moon} \end{array} \right.$

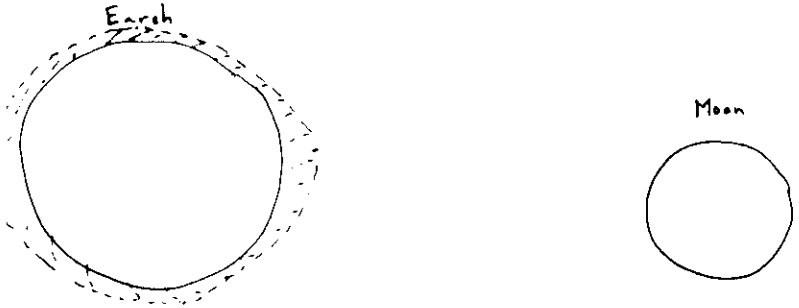


$\Longrightarrow$ A semidiurnal tide

## Solar Tides

Solar heating dominates over gravitational effects.

Solar Heating
+
Infrared Cooling


$\Rightarrow$ Diurnal + Semidiurnal + ⋮ Forcing

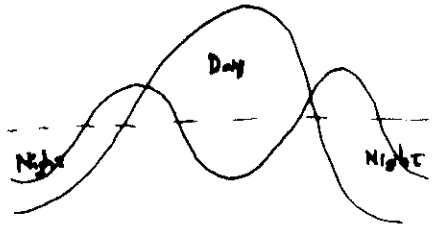


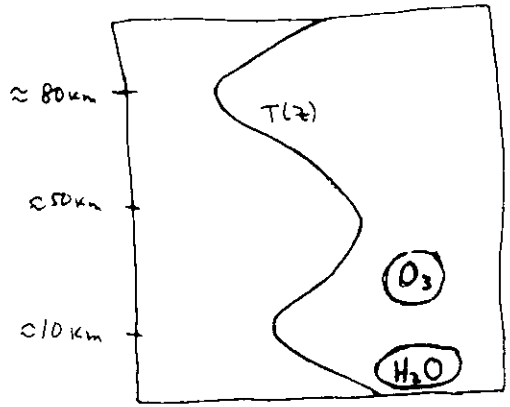


Solar heating of water vapor and ozone

## Observations

According to Haurwitz,

$$S_2(p) = 1.16 \sin^3\theta \sin(2t + 158°) + 0.085 P_2(\theta) \sin(2t_u + 118°) \text{ mbar}$$

and

$$S_1(p) \approx 0.593 \sin^3\theta \sin(t + 12°) \text{ mb}$$

where

$\theta$ = colatitude

$t_u$ = Universal Time

$$P_2(\theta) = \frac{1}{2}(3\cos^2\theta - 1)$$

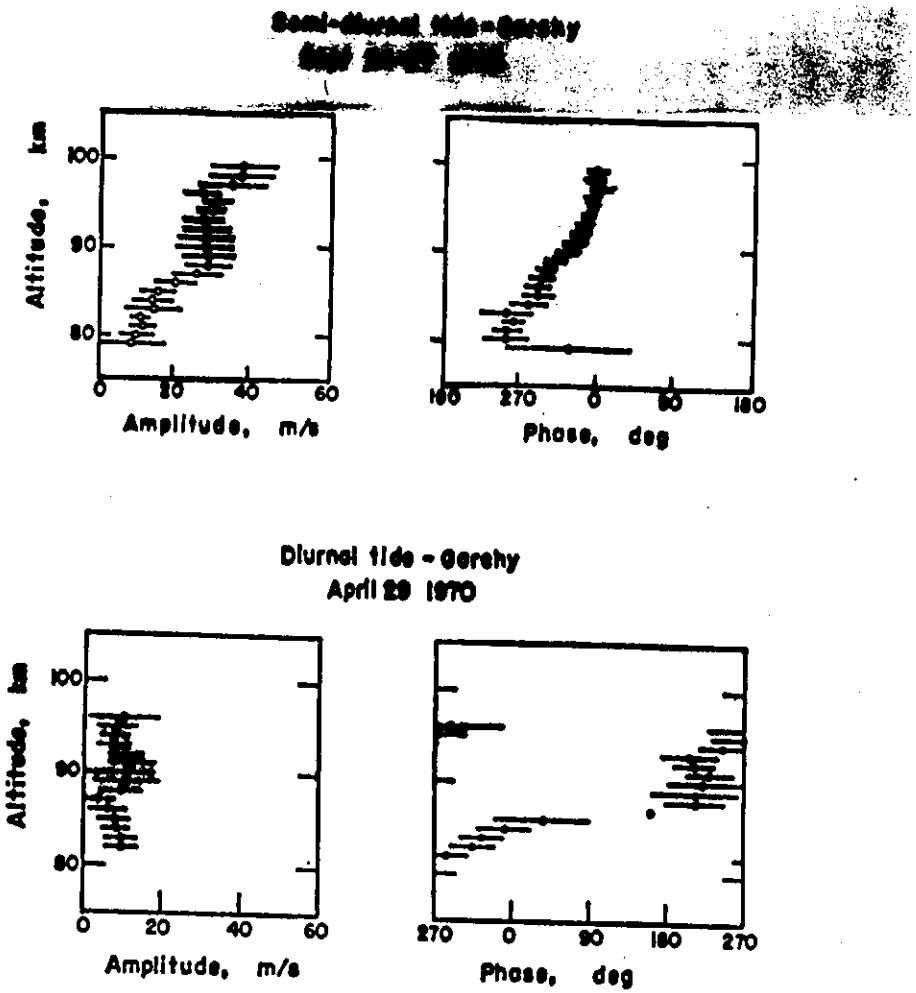


Figure 9.18: Amplitude and phase of the semidiurnal component of the eastward velocity over Garchy observed by meteor radar during September 24–7, 1970 (top), and of the diurnal component during April 29, 1970 (bottom). After Glass and Spizzichino (1974).

# Classical Tidal Theory (a brief outline)

## Two Equations

### Laplace's Tidal Equation

$$\frac{d}{d\mu}\left(\frac{1-\mu^2}{f^2-\mu^2}\frac{d\Theta_n}{d\mu}\right) - \frac{1}{f^2-\mu^2}\left[\frac{s}{f}\frac{f^2+\mu^2}{f^2-\mu^2} + \frac{s^2}{1-\mu^2}\right]\Theta_n + \frac{4a^2\Omega^2}{gh_n}\Theta_n = 0$$

where

$$\mu = \cos\theta$$

### Vertical Structure Equation

$$\frac{d^2\tilde{w}_n}{dz^{*2}} + \left[\frac{R}{gh_n}\left(\frac{dT_0}{dz} + \frac{RT_0}{c_p}\right) - \frac{1}{4}\right]\tilde{w}_n = \frac{\varkappa J_n}{gh_n} e^{-\frac{z^*}{2}}$$

where $z^* \equiv -\ln\left(\frac{p}{p_s}\right)$

and $w^* = \frac{dz^*}{dt}$

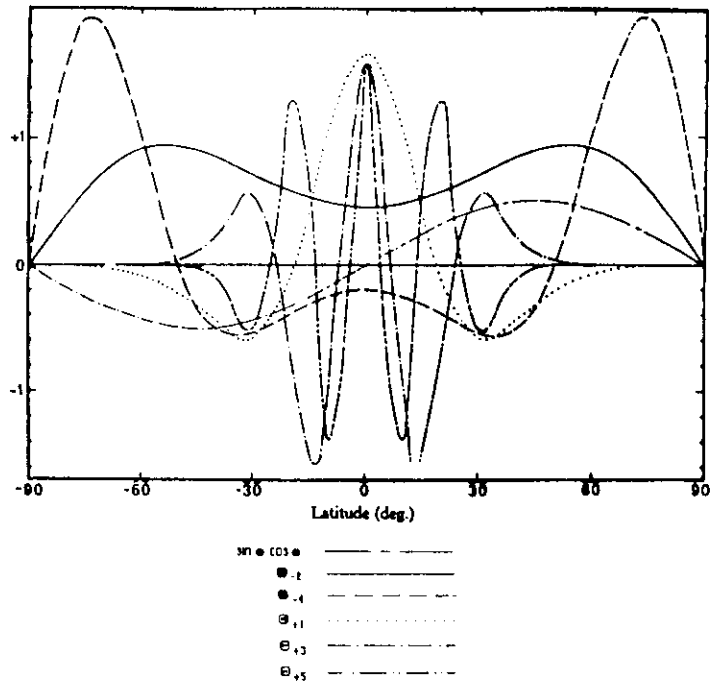


Figure 9.25: Symmetric Hough functions for the migrating solar diurnal thermal tide. Also shown is $\sin\theta\cos\theta$, the most important odd mode. After Lindzen (1967b).

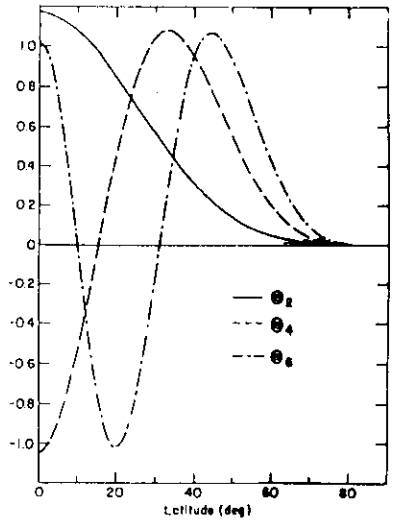


Figure 9.24: Latitude distribution for the first three symmetric solar semidiurnal migrating Hough functions. After Chapman and Lindzen (1970).

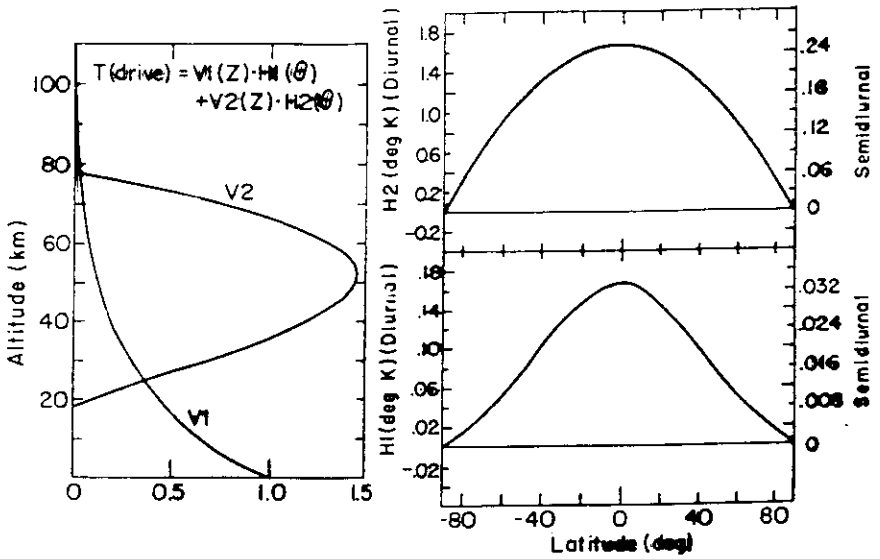


Fig. 3.2. Vertical distributions of thermal excitation due to water vapor (V1) and ozone (V2); latitude distributions for water vapor (H1) and ozone (H2). After Lindzen (1968a).

Now, $\tau_G^{\sigma,s} = \dfrac{\varkappa J_G^{\sigma,s}}{i\sigma R}$ and

$\tau = \sum_G \sum_{n=1}^{\infty} \tau_G^{n\sigma,n}(z,\theta)\, e^{int}$ where $\tau_G^{\sigma,s} = f_G^{\sigma,s}(z)\, g_G^{\sigma,s}(\theta)$

Diurnal

$H_{O_3}^{D} = 1.63\,^{\circ}K\,\Theta_{-2}^{D} - 0.51\,^{\circ}K\,\Theta_{-1}^{D} + \cdots$

$+ 0.54\,^{\circ}K\,\Theta_{1}^{D} - 0.14\,^{\circ}K\,\Theta_{3}^{D} + \cdots$

$H_{H_2O}^{D} = 0.16\,^{\circ}K\,\Theta_{-2}^{D} - 0.055\,^{\circ}K\,\Theta_{-1}^{D} + \cdots$

$+ 0.62\,^{\circ}K\,\Theta_{1}^{D} - 0.016\,^{\circ}K\,\Theta_{3}^{D} + \cdots$

Semidiurnal

$H_{O_3}^{S\text{-}D} = 0.25\,^{\circ}K\,\Theta_{2}^{S\text{-}D} + 0.065\,^{\circ}K\,\Theta_{4}^{S\text{-}D} + 0.036\,^{\circ}K\,\Theta_{6}^{S\text{-}D} + \cdots$

$H_{H_2O}^{S\text{-}D} = 0.031\,^{\circ}K\,\Theta_{2}^{S\text{-}D} + 0.008\,^{\circ}K\,\Theta_{4}^{S\text{-}D} + 0.0045\,^{\circ}K\,\Theta_{6}^{S\text{-}D} + \cdots$

Table 9.1:

| Diurnal Mode # | $h_n$ | Semidiurnal Mode # | $h_n$ |
|---|---|---|---|
| + 1 | .69 km | 2 | 7.85 km |
| + 3 | .12 km | 4 | 2.11 km |
| + 5 | .05 km | 6 | 0.96 km |
| - 2 | -12.27 km | | |
| - 4 | -1.76 km | | |

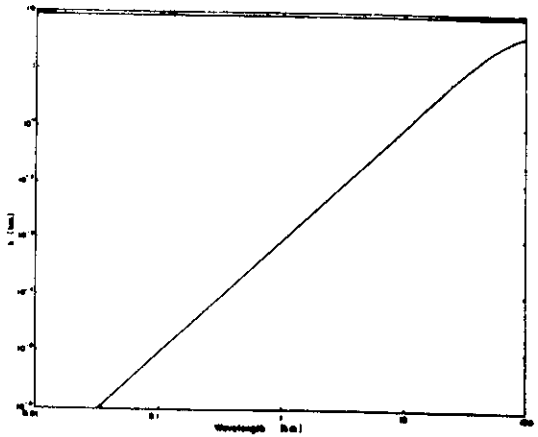

Figure 9.22: Vertical wavelength as a function of equivalent depth. After Lindzen (1967b).

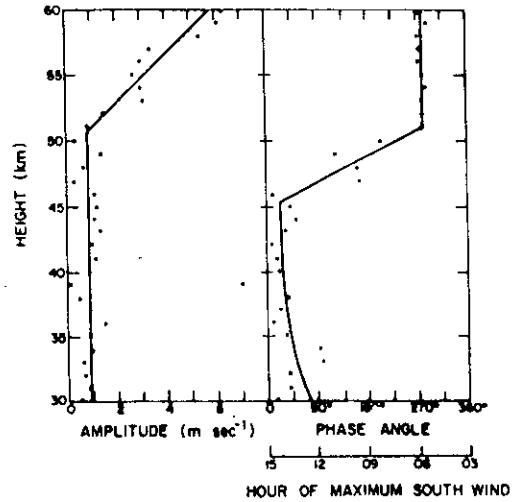


Figure 9.15: Phase and amplitude of the semidiurnal variation of the meridional wind component u at 30°N based on data from White Sands (32.4°N) and Cape Kennedy (28.5°N). After Reed (1967).

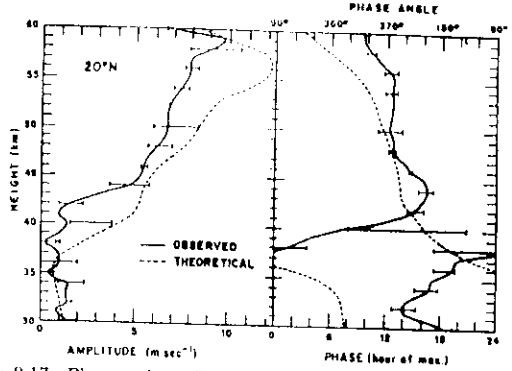


Figure 9.17: Phase and amplitude of the diurnal variation of the meridional wind component $u$ at 20°N. Phase angle, in accordance with the usual convention, gives the degrees in advance of the origin (chosen as midnight) at which the sine curve crosses from − to +. The theoretical curves will be discussed later in this chapter. After Reed *et al.* (1969).

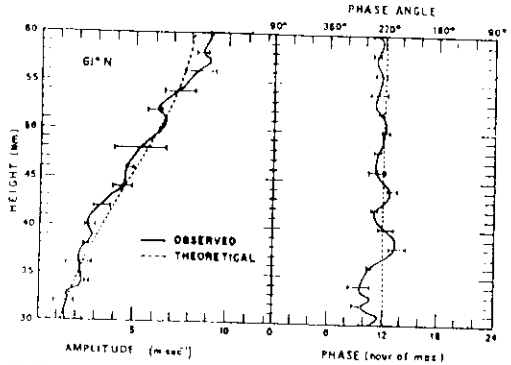


Figure 9.16: Phase and amplitude of the diurnal variation of the meridional wind component $u$ at 61°N. Phase angle, in accordance with the usual convention, gives the degrees in advance of the origin (chosen as midnight) at which the sine curve crosses from − to +. The theoretical curves will be discussed later in this chapter. After Reed *et al.* (1969)

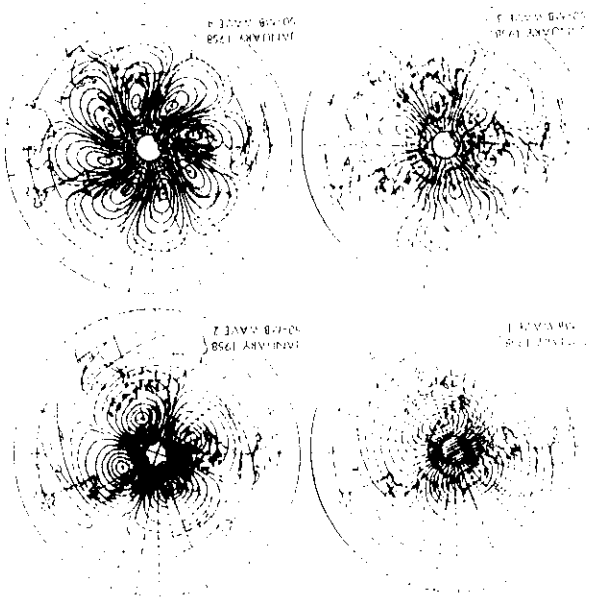

Fig. 10. 50-mb standing waves 1 through 4 for January 1958 (after Ref. 6)

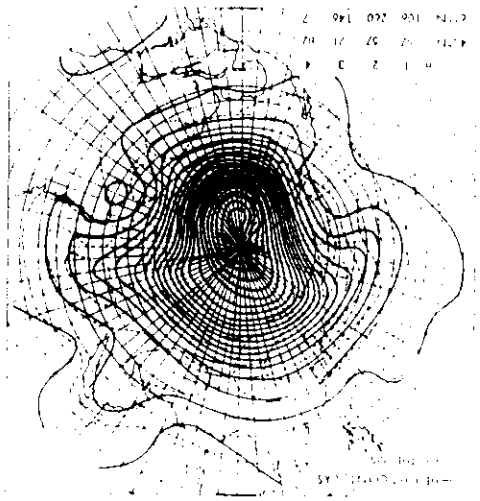

Fig. 9. Northern Hemisphere 50-mb chart for 1200 GMT, January 13, 1958. Height contours are given in meters, isotherms in °C. Amplitudes of wave numbers 1 through 4 are tabulated in meters at the bottom of the map (from Ref. 6)

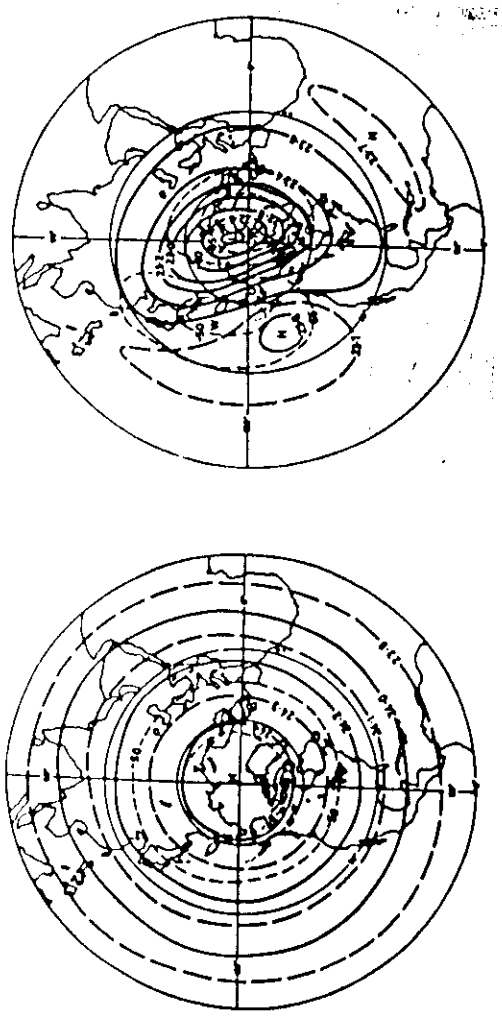

Fig. 11.2 Mean 30-mb geopotential height (solid lines, km) and temperature (dashed lines, °C) for Northern Hemisphere summer (left) and winter (right) averaged for 1958–1961. (After Hare, 1968.)

Charney and Drazin (1961) pioneered studying the vertical propagation of atmospheric planetary waves. They showed the following:

(1) vertical propagation of planetary waves cannot take place in regions where the mean zonal winds are either easterly or very large and westerly;

(2) short wavelength waves cannot propagate vertically; and

(3) the second-order effect of small amplitude stationary planetary waves on the mean zonal flow is zero in the absence of diabatic effects and zero wind lines.

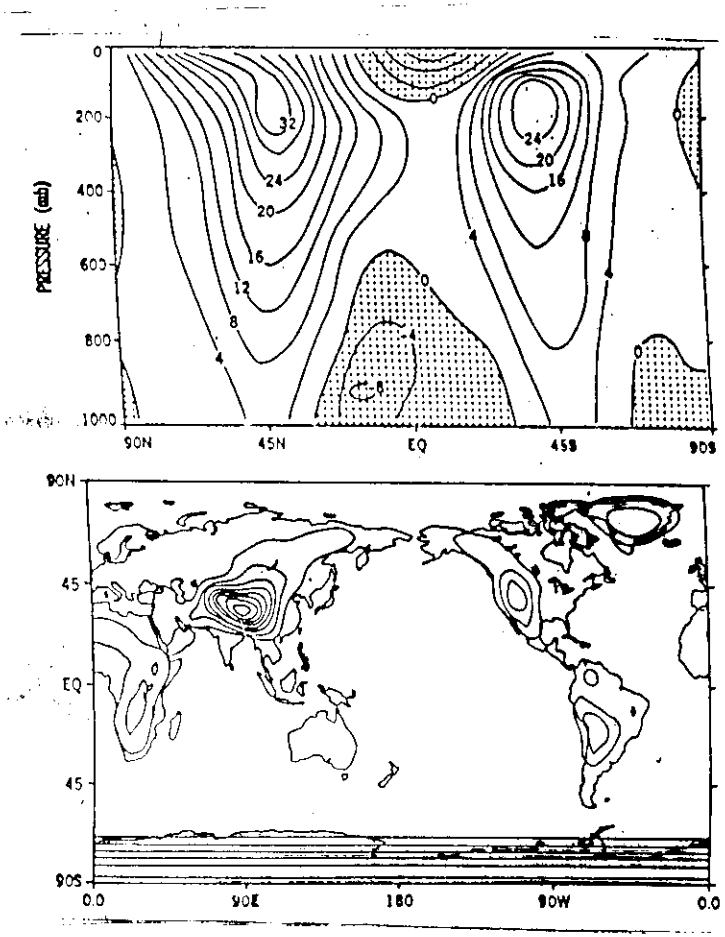


Figure 1. Top - Latitude-pressure plot of the wintertime zonally averaged zonal wind from GCM simulation. Bottom - Orography distribution where the contour interval is 500 m and the zero contour is not shown (eddy topography south of 65 °S has been set to zero). Taken from Nigam et al. (1988).

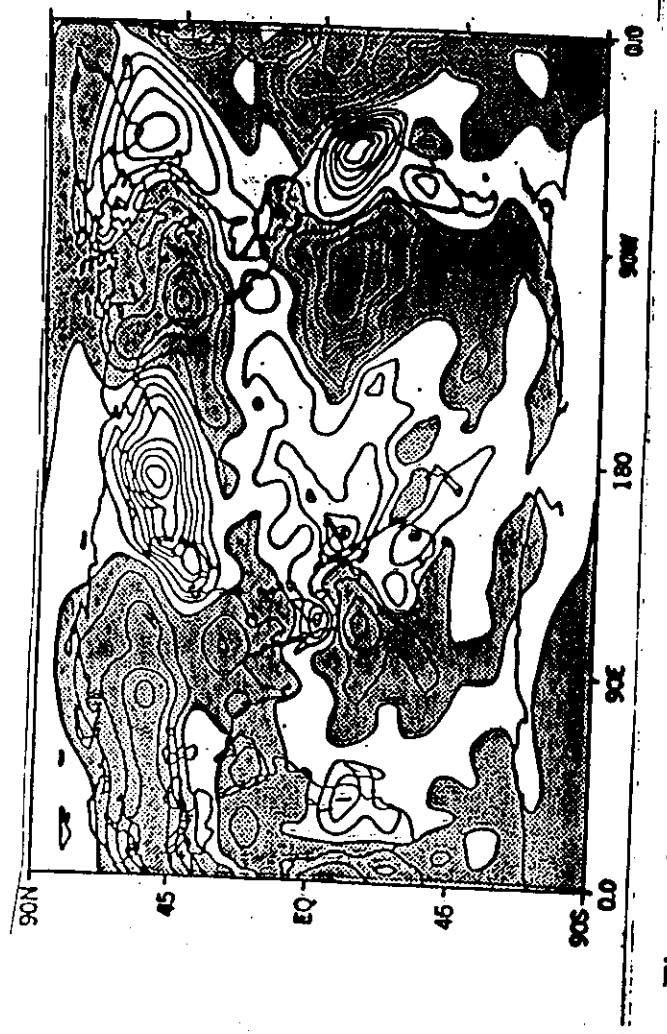


Figure 2. The vertically averaged heating rate for the wintertime GCM simulation of Nigam et al. (1986).

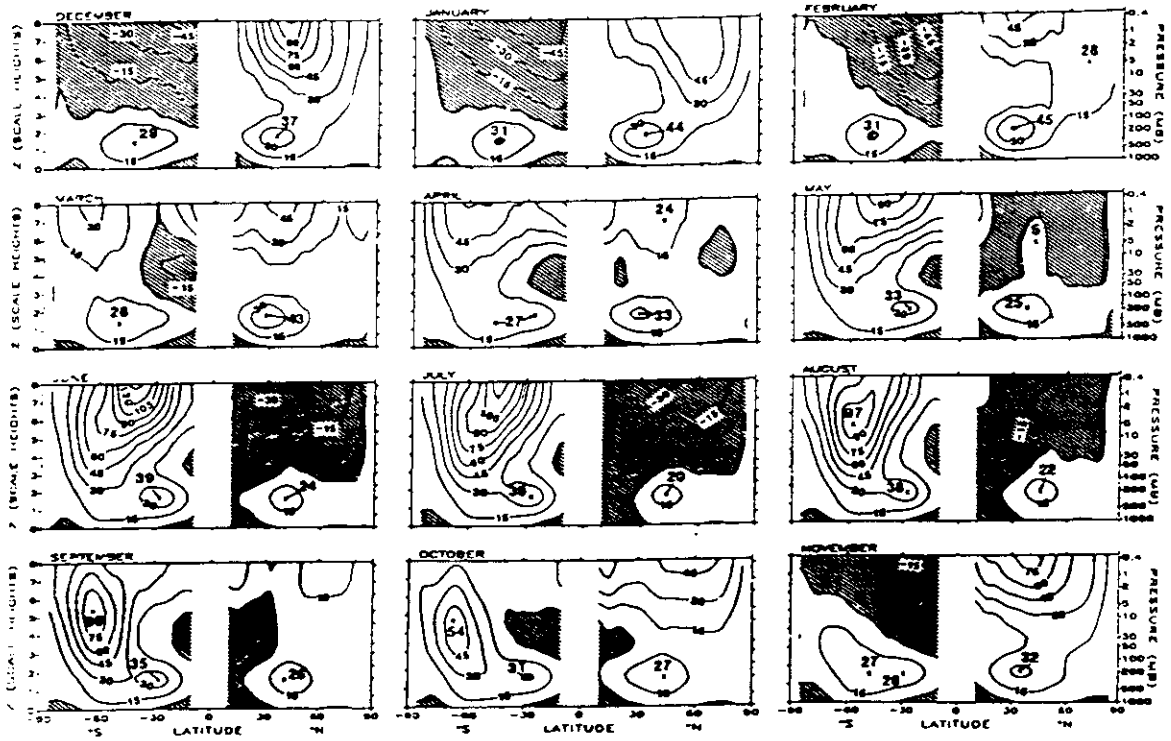


Figure 12. Monthly mean zonal winds (in m/s) for the twelve months of the year. Taken from Geller and Wu (1987).

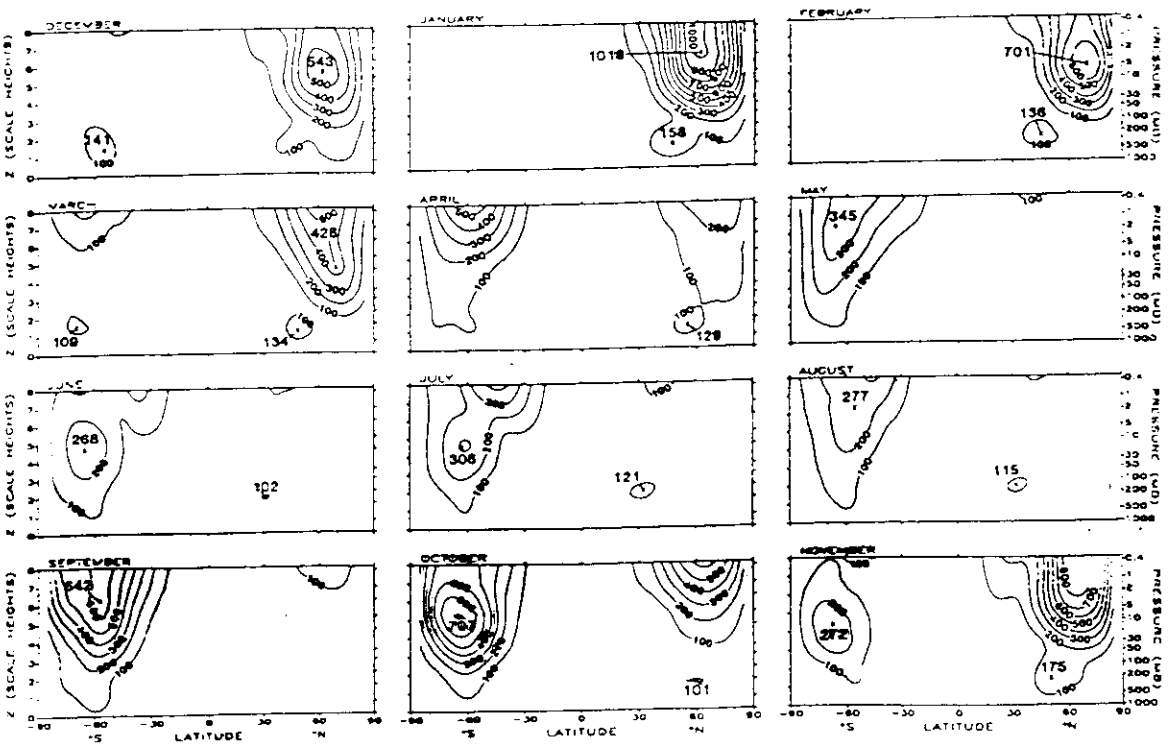


Figure 13: Amplitudes for the monthly mean wavenumber 1 in geopotential height (in meters) for the twelve months of the year. Taken from Geller and Wu (1987).

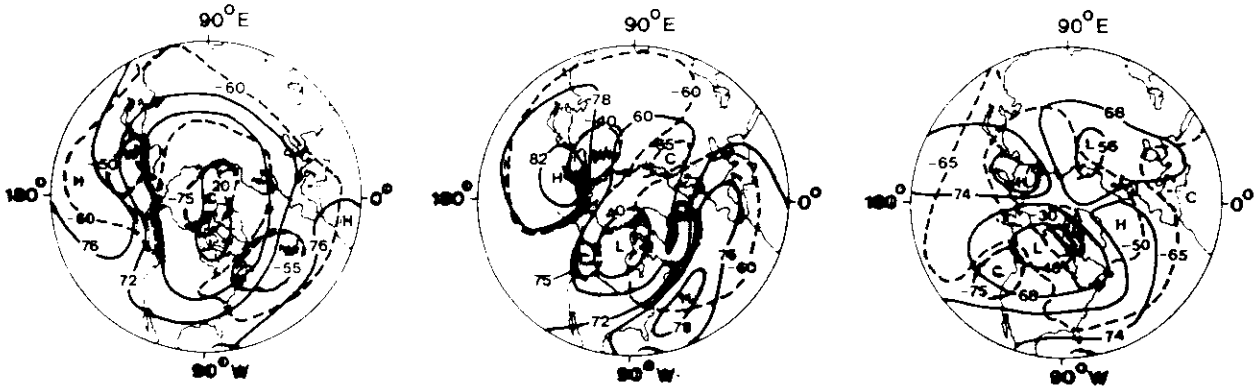


Fig. 3. 50 mb charts showing evolution of the sudden stratospheric warming of early 1957. Contours (full line) in 100's of feet; isotherms (dashed lines) in deg C (adapted from (6)).

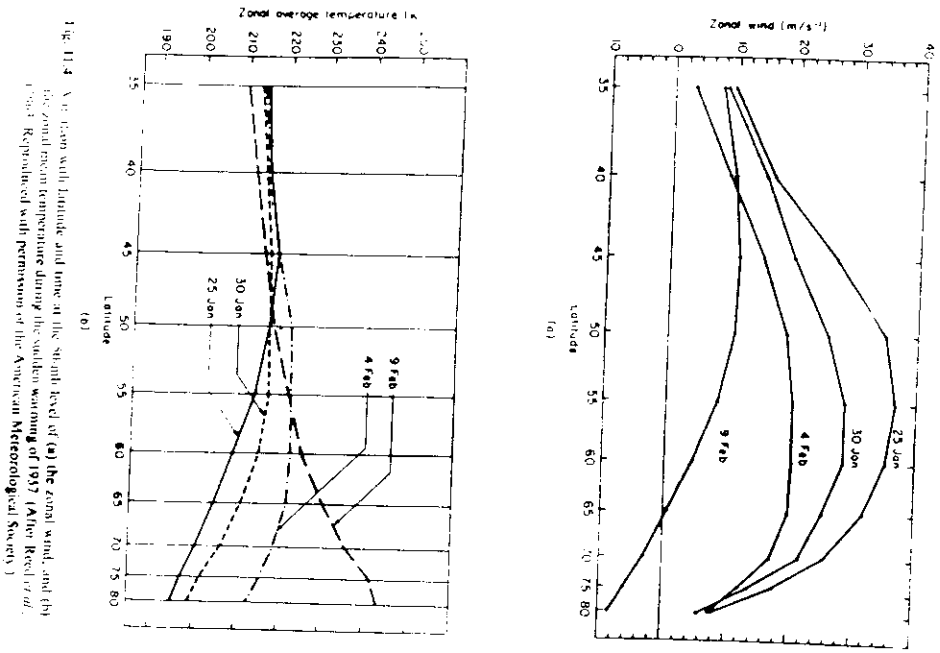


Fig. 11.4 Variation with latitude and time at the 50 mb level of (a) the zonal wind, and (b) the zonal mean temperature during the sudden warming of 1957 (After Reed *et al.*, 1958). Reproduced with permission of the American Meteorological Society.)

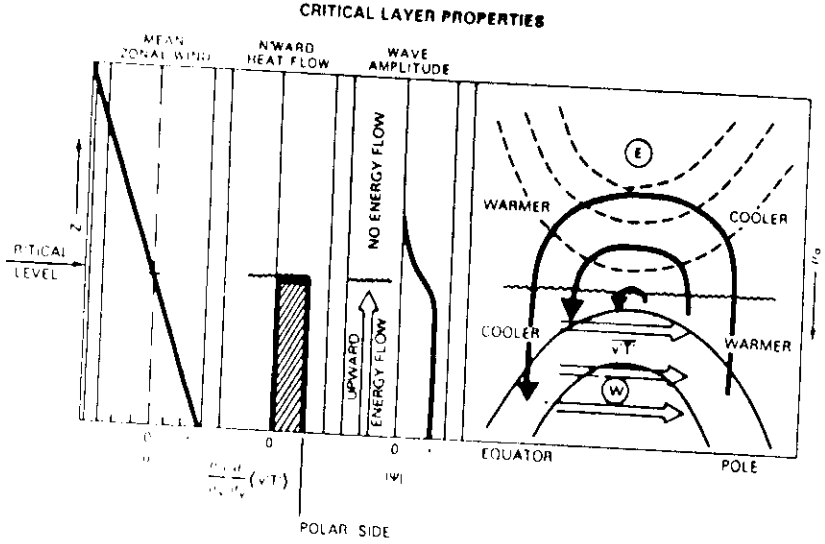


[illegible] critical layer properties for a stratospheric warming. From left to right the figure shows the mean zonal wind at midchannel, the meridional derivative of the northward heat flow as a function of height along the polar side of the channel, and the wave amplitude and energy flow at midchannel. The diagram on the far right shows the two-dimensional idealized structure of a critical layer. Open arrows indicate the direction of eddy heat transport. Solid arrows show cross-channel and vertical flow patterns, the induced secondary circulation. Contours indicate zonal winds; dashed lines are easterly, and solid lines are westerly (from [4]).

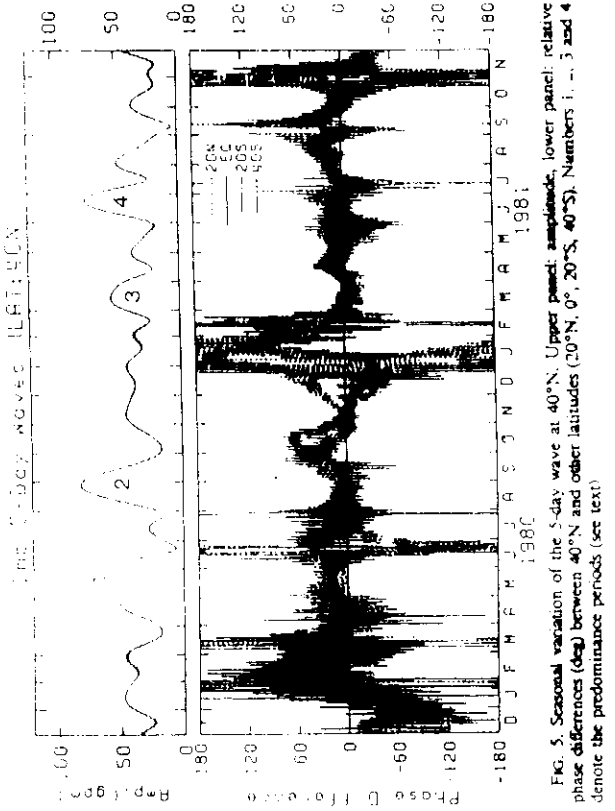


FIG. 5. Seasonal variation of the 5-day wave at 40°N. Upper panel: amplitude, lower panel: relative phase differences (deg) between 40°N and other latitudes (20°N, 0°, 20°S, 40°S). Numbers 1, 2, 3 and 4 denote the predominance periods (see text).

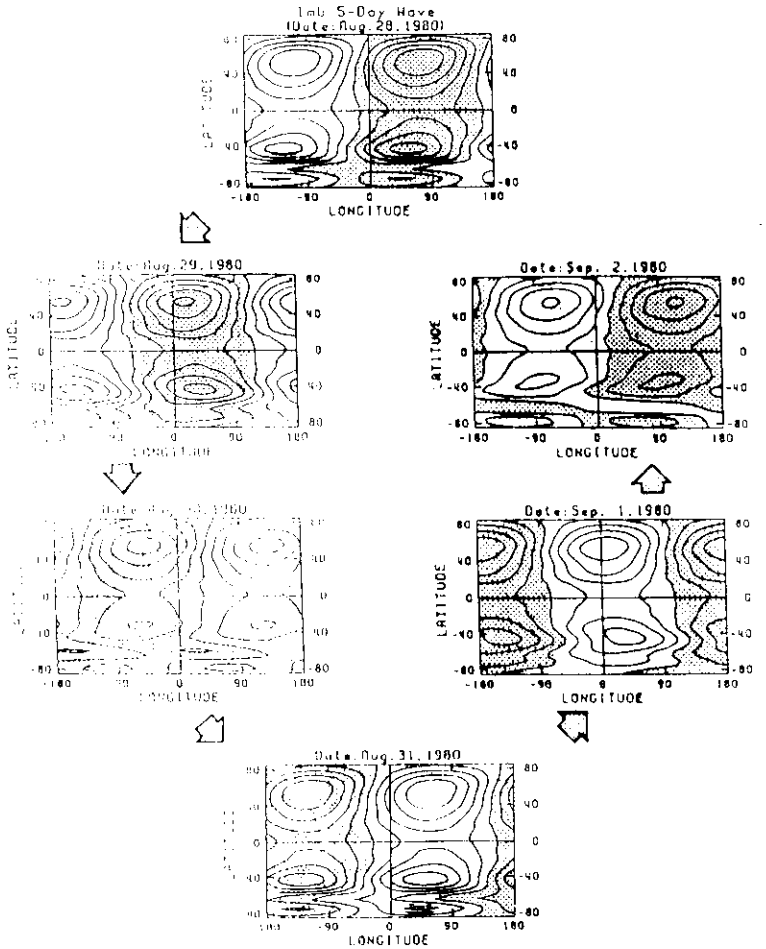


Fig. [illegible] geopotential at the 1 mb 5 day wave for the six successive days of 28 August–2 September 1980. Shaded regions denote negative anomalies. The contour interval is 20 m.

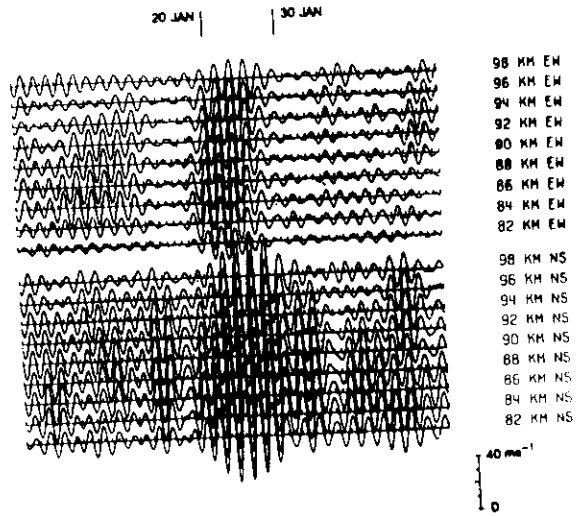


Fig. 1. Eastward (top) and northward (bottom) components of the winds observed at Adelaide between 82 and 98 km during January and early February 1984. Data have been band-pass filtered to retain only periods between 30 and 80 h. Scale at lower right. Tick marks on axes denote daily intervals.

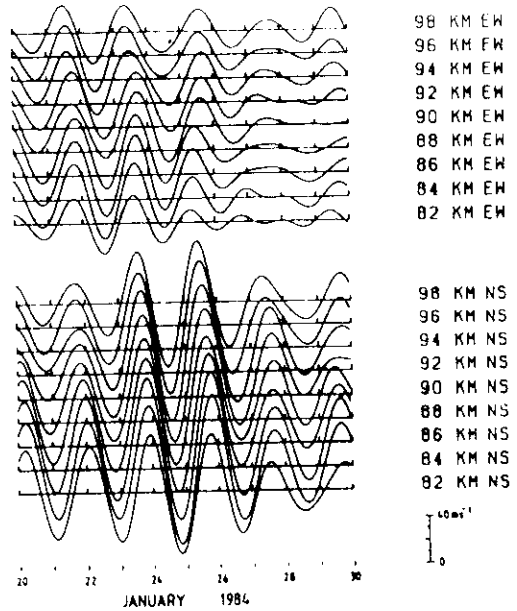


Fig. 2. Expanded plot of Fig. 1 for the period 20–30 January 1984.

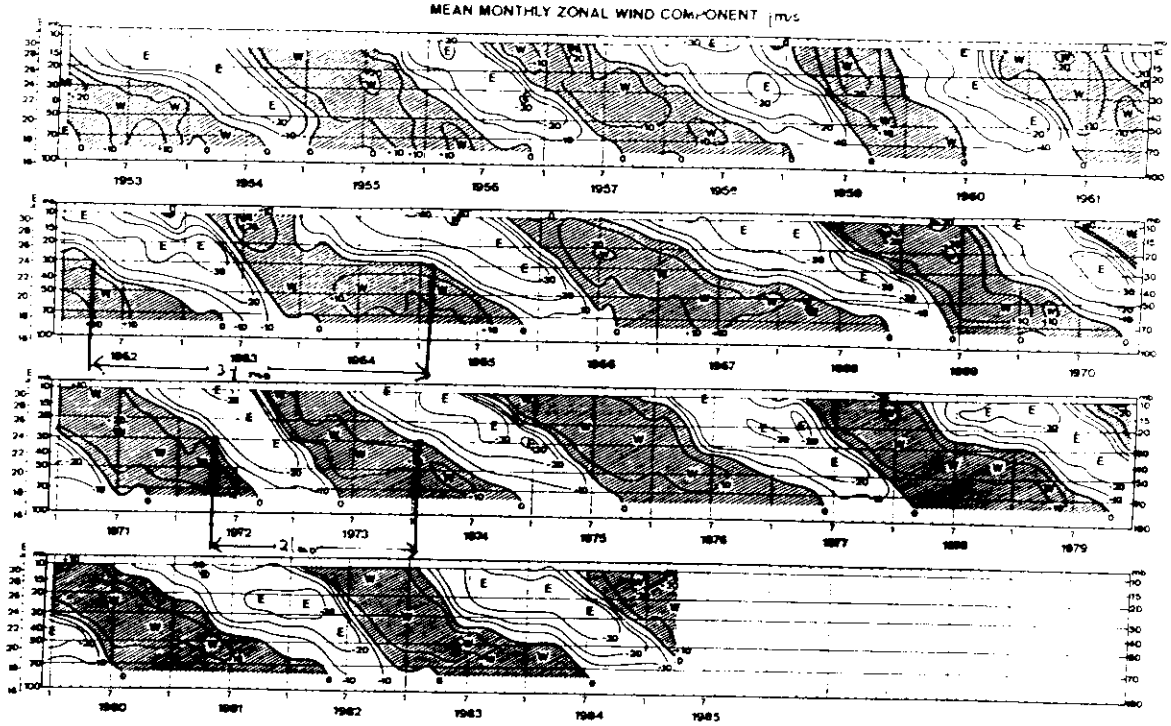


**Figure 6-28.** Time-height cross section of mean monthly zonal winds (m/s) at equatorial stations, calculated from all available daily values:
Jan 1953 - Aug 1967 Canton Island, 3°S/172°W
Sep 1967 - Dec 1975 Gan/Maledive Islands, 1°S/73°E
Jan 1976 - Apr 1985 Singapore, 1°N/104°E (After Naujokat, 1985)

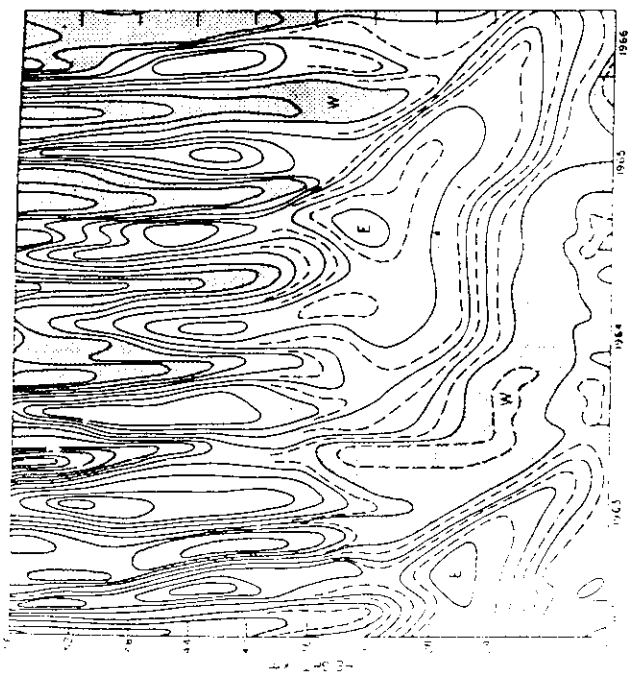

Fig. 4 Time-height section of zonal wind at 8° latitude with annual cycle removed. Solid isotachs are placed at intervals of 10 m sec$^{-1}$. Shaded areas indicate westerlies. Below 35 km, monthly mean rawinsonde data for the Canal Zone (9°N) and Ascension Island (8°S) were averaged together to remove all fluctuations with odd symmetry about the equator. Above 35 km this procedure could not be used because rocket data were only available for Ascension Island. At these levels the annual cycle was removed by Fourier analysis. Some minor smoothing was done to make the analyses compatible at 35 km.

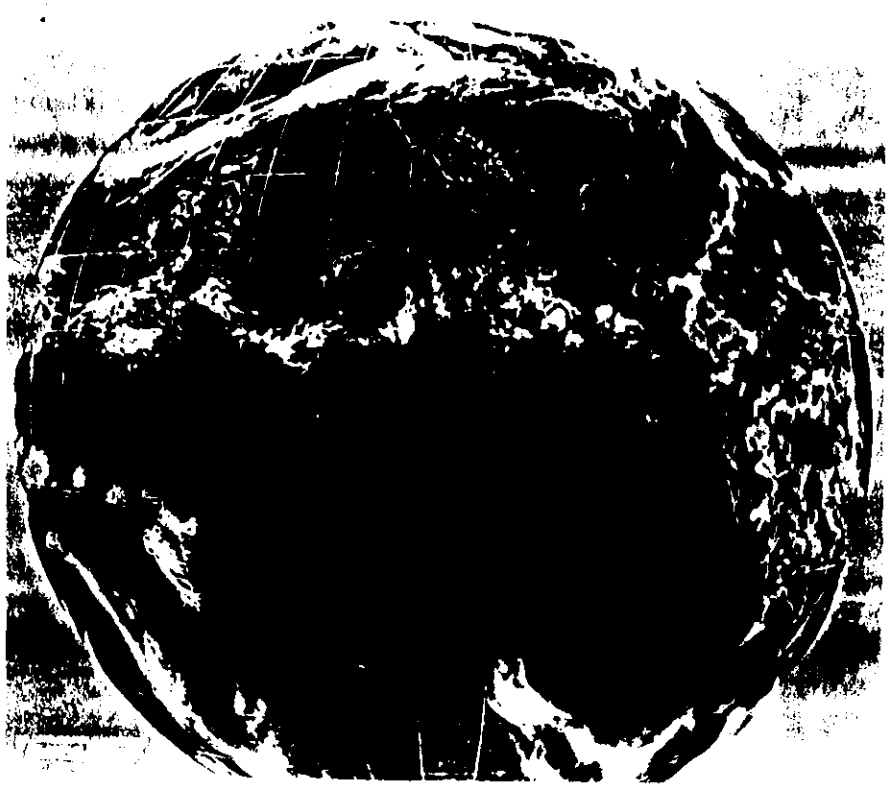

**Figure 5. Infrared geostationary satellite picture for October 20, 1975. Latitude and longitude interval is 10 degrees (solid lines). About one-third of the globe is visible. Note that there are about 10 cloud clusters seen in the band located in the Equatorial Trough Zone.**

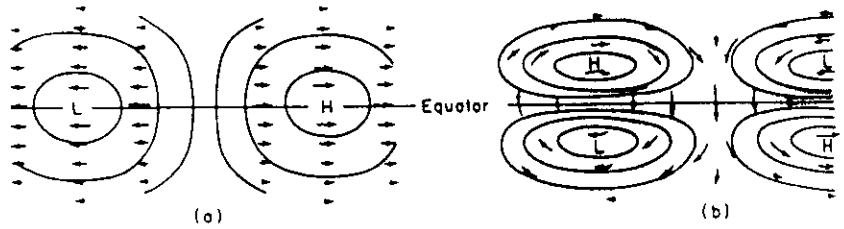


Fig. 11.7 Velocity and pressure distributions in the horizontal plane for (a) Kelvin waves, and (b) mixed Rossby–gravity waves. (After Matsuno, 1966.)

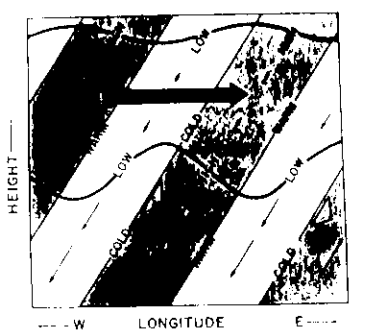


Fig. 11.8a Longitude–height section along the equator showing pressure, temperature, and wind perturbations for a thermally damped Kelvin wave. Heavy wavy lines indicate material lines, short blunt arrows show phase propagation. Areas of high pressure are shaded. Length of the small thin arrows is proportional to the wave amplitude which decreases with height due to damping. The large shaded arrow indicates the net mean flow acceleration due to the wave stress divergence.

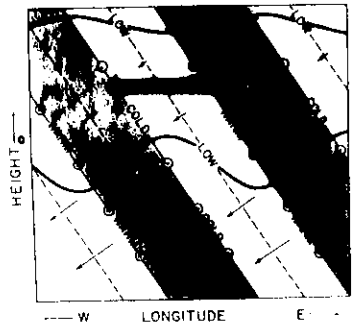


Fig. 11.8b Longitude–height section along a latitude circle north of the equator showing pressure, temperature, and wind perturbations for a thermally damped mixed Rossby–gravity wave. Areas of high pressure are shaded. Small arrows indicate zonal and vertical wind perturbations with length proportional to the wave amplitude. Meridional wind perturbations are shown by arrows pointed into the page (northward) and out of the page (southward). The large shaded arrow indicates the net mean flow acceleration due to the wave stress divergence.

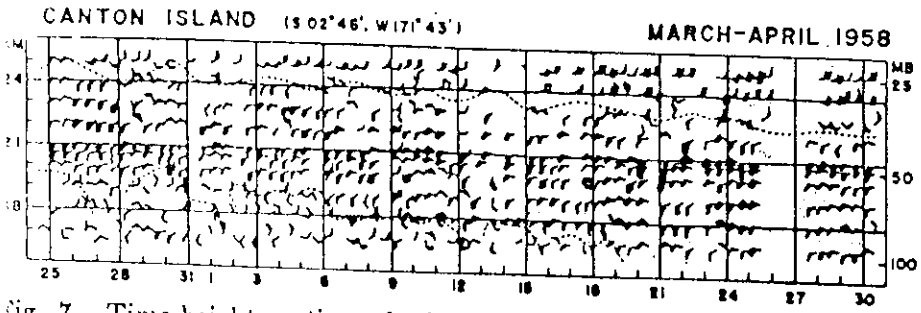


Fig. 7. Time-height section of wind in knots (adapted from *Maruyama and Yanai* [1967]). Shaded regions denote southerly components.

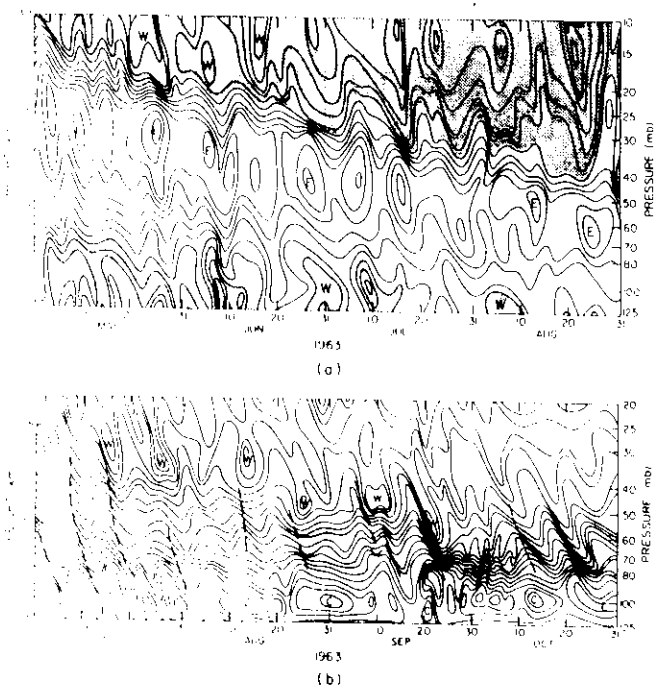


Fig. 4.25. Time-height sections for the equatorial lower stratosphere, showing evidence of Kelvin wave activity. (a) Zonal wind and (b) temperature at Canton Island (3°S). Note the westerly phase of the QBO encroaching from upper levels in (a). see Chapter 8. [From Giu (1982).]

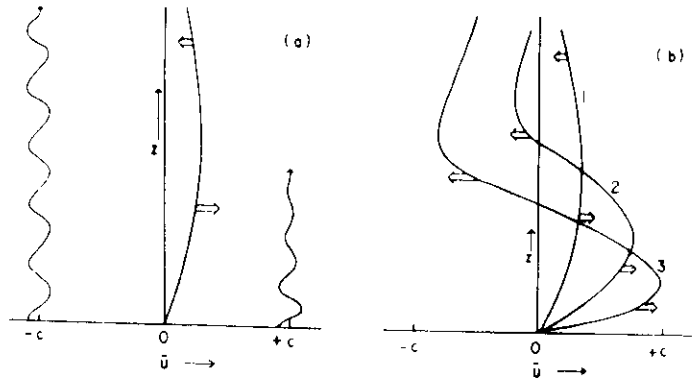


Fig. 8.6. Schematic representation of the instability of zonal flow in a stratified fluid with standing-wave forcing at a lower boundary. (a) Onset of instability from a small zonal flow perturbation. (b) Early stages of the subsequent mean-flow evolution. Broad arrows show locations and direction of maxima in mean wind acceleration. Wavy lines indicate relative penetration of wave components of positive and negative phase speeds c. [From Plumb (1982), with permission.]

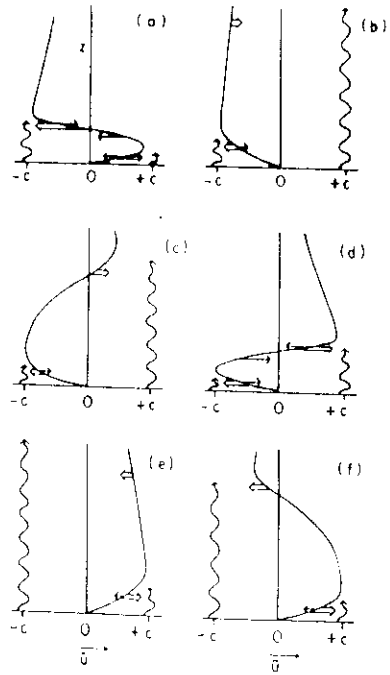


Fig. 8.7. Schematic representation of the evolution of the mean flow in Plumb's a the QBO. Six stages of a complete cycle are shown. Double arrows show wav accelerations and single arrows show viscously driven accelerations. Wavy lines indicate penetration of easterly and westerly waves. See text for details. [After Plumb (1984).]

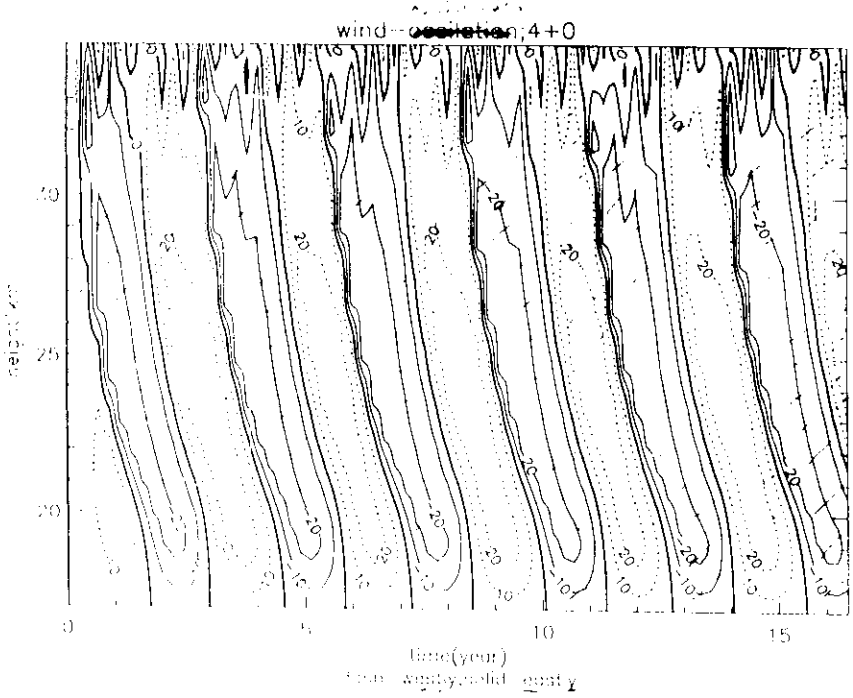
wind oscillation,4+0
time(year)

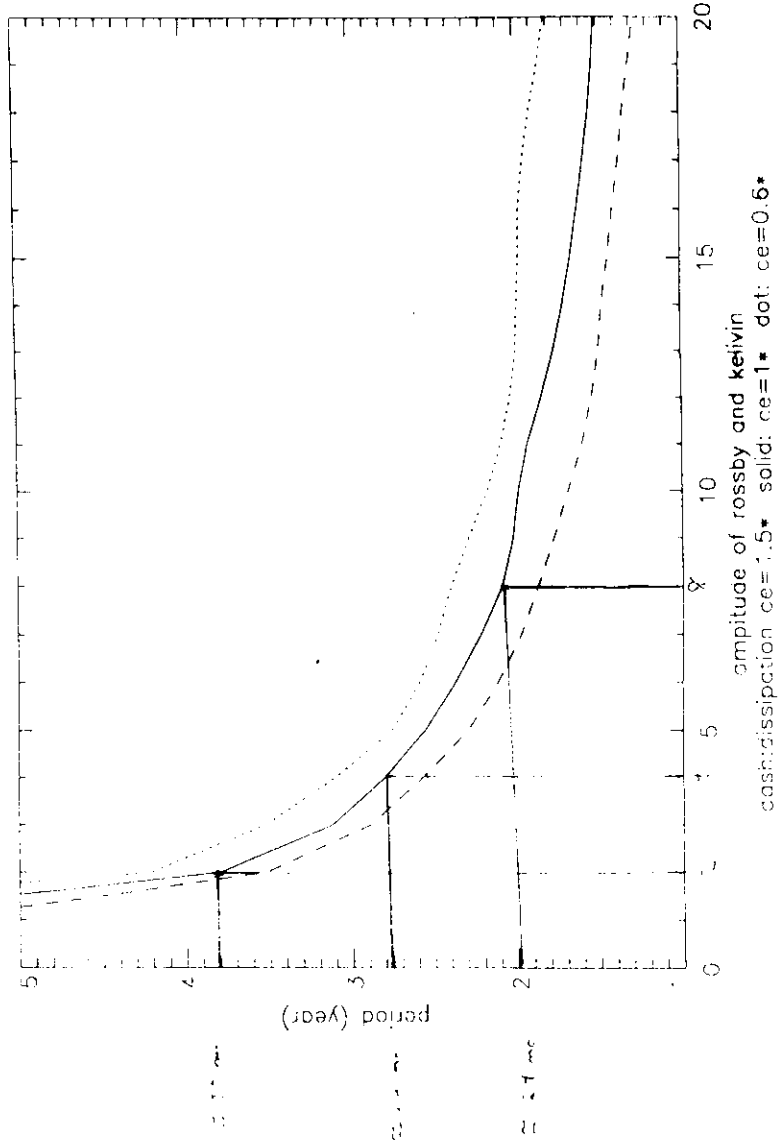
amplitude of rossby and kelvin
period (year)

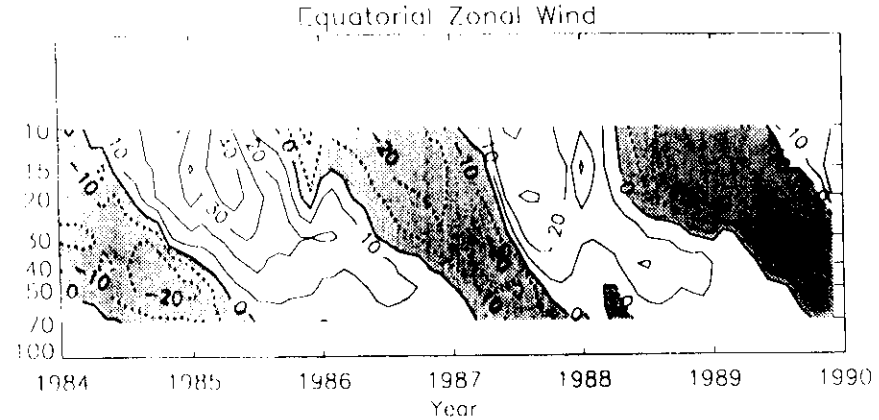
Equatorial Zonal Wind
10
15
20
30
40
50
70
100
1984
1985
1986
1987
1988
1989
1990
Year

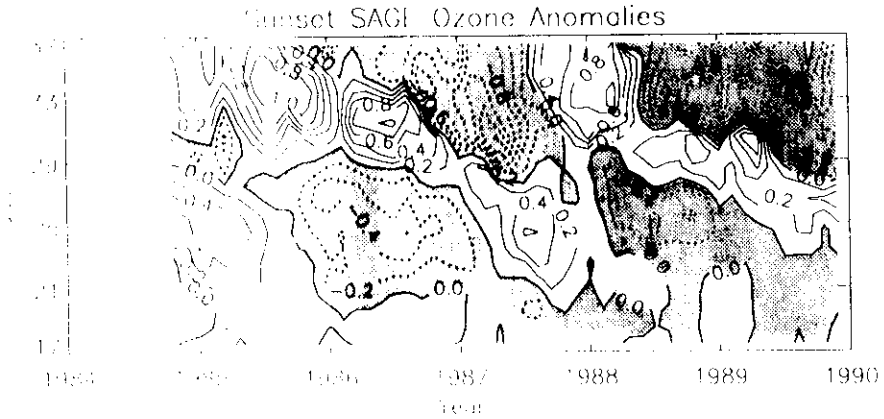
Sunset SAGE Ozone Anomalies
1984
1985
1986
1987
1988
1989
1990
Year

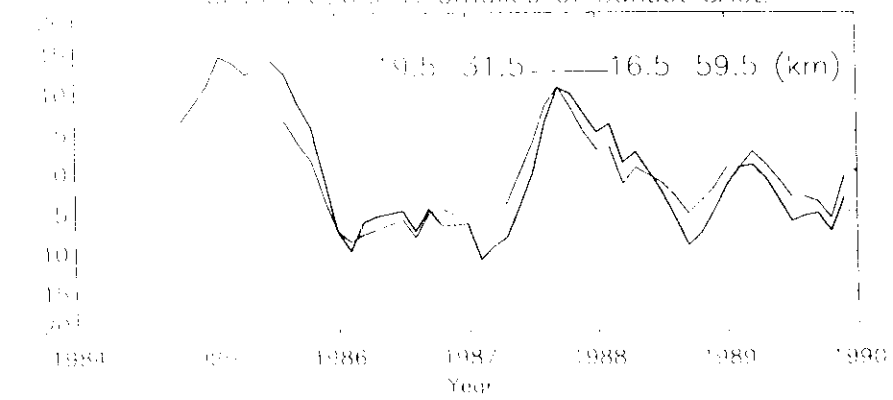
Ozone Anomalies of Sunset SAGE
16.5 31.5
16.5 59.5 (km)
1984
1986
1987
1988
1989
1990
Year

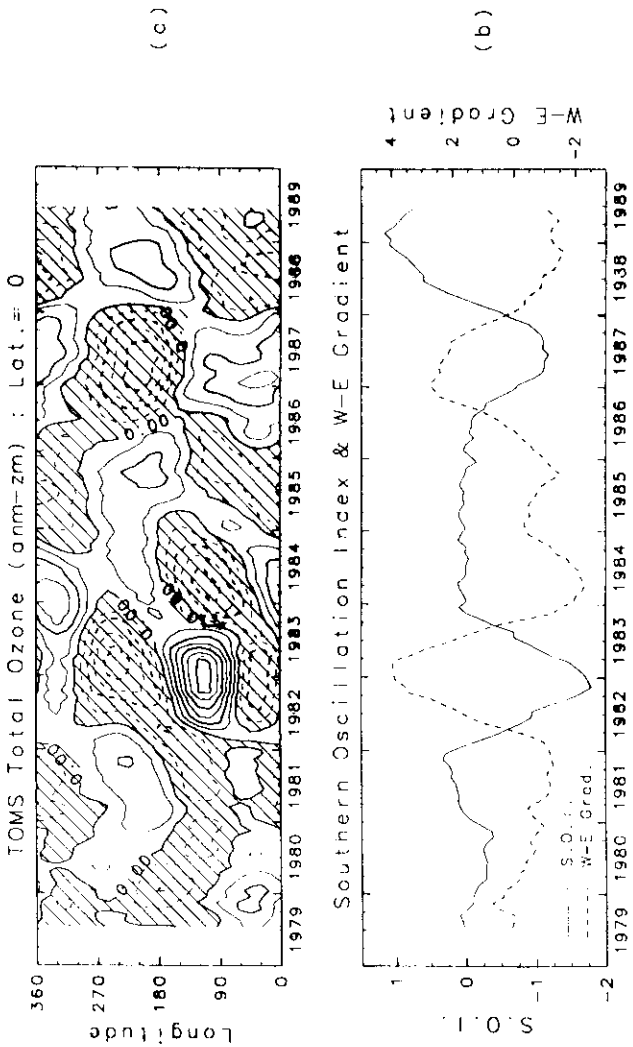
(c)
TOMS Total Ozone (anm-zm) : Lat.= 0
Longitude
360
270
180
90
0
1979
1980
1981
1982
1983
1984
1985
1986
1987
1988
1989
(b)
Southern Oscillation Index & W-E Gradient
W-E Gradient
4
2
0
-2
S.O.I.
1
0
-1
-2
S.O.I.
W-E Grad.